Available online at www.sciencedirect.com
ScienceDirect
ELSEVIER
Icarus ••• (••••) •••–•••
ICARUS
www.elsevier.com/locate/icarus

Ground-based near infrared spectroscopy of Jupiter's ring and moons

Michael H. Wong [a,*], Imke de Pater [a], Mark R. Showalter [b], Henry G. Roe [c], Bruce Macintosh [d], Giuli Verbanac [e]

[a] *Astronomy Department, 601 Campbell Hall, University of California, Berkeley, CA 94720-3411, USA*
[b] *SETI Institute, 515 N Whisman Road, Mountain View, CA 94043, USA*
[c] *Division of Geological and Planetary Sciences, California Institute of Technology, Pasadena, CA 91125, USA*
[d] *Institute of Geophysics and Planetary Physics, Lawrence Livermore National Laboratory, Livermore, CA 94550, USA*
[e] *Faculty of Science, University of Zagreb, Horvatovac bb, 10000 Zagreb, Croatia*

Received 31 October 2005; revised 30 May 2006

Abstract

The backscattered reflectivity of Jupiter's ring has been previously measured over distinct visible and near infrared wavelength bands by a number of ground-based and spaceborne instruments. We present spectra of Jupiter's main ring from 2.21–2.46 μm taken with the NIRSPEC spectrometer at the W.M. Keck observatory. At these wavelengths, scattered light from Jupiter is minimal due to the strong absorption of methane in the planet's atmosphere. We find an overall flat spectral slope over this wavelength interval, except for a possible red slope shortward of 2.25 μm. We extended the spectral coverage of the ring to shorter wavelengths by adding a narrow-band image at 1.64 μm, and show results from 2.27-μm images over phase angles of 1.2°–11.0°. Our images at 1.64 and 2.27 μm reveal that the halo contribution is stronger at the shorter wavelength, possibly due to the redder spectrum of the ring parent bodies as compared with the halo dust component. We find no variation in main ring reflectivity over the 1.2°–11.0° phase angle range at 2.27 μm. We use adaptive optics imaging at the longer wavelength L′ band (3.4–4.1 μm) to determine a 2-σ upper limit of 22 m of vertically-integrated I/F. Our observing campaign also produced an L′ image of Callisto, showing a darker leading hemisphere, and a spectrum of Amalthea over the 2.2–2.5 and 2.85–3.03 μm ranges, showing deep 3-μm absorption.

Keywords: Planetary rings; Jupiter; Infrared observations; Spectroscopy; Jupiter, satellites

1. Introduction

Jupiter's ring was first detected when Pioneer 11 recorded drops in the energetic particle flux corresponding to the 1.7–1.8 R_J region (Fillius et al., 1975; Acuña and Ness, 1976). This flux anomaly provides the only direct evidence found so far for the existence of large (>5 cm) particles in Jupiter's ring (Ip, 1980), although these large particles are often invoked as parent bodies for the more plentiful small particles that show up in scattered sunlight. The Voyager spacecraft were the first to detect the rings in reflected sunlight, and were able to distinguish the three main components of the ring system: the main ring, the halo, and the gossamer rings (Owen et al., 1979; Jewitt and Danielson, 1981; Burns et al., 1984; Showalter et al., 1985, 1987). The main ring has a north–south thickness of no more than 30 km as seen in back-scattered sunlight, and a radial width of 6000–7000 km (Ockert-Bell et al., 1999; Showalter et al., 1987), spanning 1.72 to 1.81 R_J, with 1 R_J = 71,398 km from Smoluchowski (1976). The main ring has a normal optical depth $\tau_\perp$ of a few $\times 10^{-6}$, depending on the wavelength, as determined by a number of spacecraft and ground-based photometric studies (see the review by Throop et al., 2004). The halo extends from an inner radius of about 1.4 R_J out to the main ring, and has a north–south thickness of 2×10^4 km. The halo has a normal optical depth comparable to the main ring ($\tau_\perp \approx 10^{-6}$), but its extended structure makes it more difficult to observe (Showalter et al., 1987). The gossamer rings extend beyond the main ring to just past Thebe's

* Corresponding author. Fax: +1 510 642 3411.
E-mail addresses: mikewong@astro.berkeley.edu (M.H. Wong), imke@berkeley.edu (I. de Pater), mshowalter@seti.org (M.R. Showalter), hroe@gps.caltech.edu (H.G. Roe), bmac@igpp.ucllnl.org (B. Macintosh), verbanac@irb.hr (G. Verbanac).

0019-1035/$ – see front matter
doi:10.1016/j.icarus.2006.07.007

orbit at 3.11 R_J and are the optically thinnest component of the jovian ring system, with $\tau_\perp < 10^{-8}$ in backscattered sunlight at 2.27 μm (de Pater et al., 1999).

An abundance of fine dust in the ring system is evident from the much brighter forward-scattered appearance of the ring in Voyager, Galileo, and Cassini images, as compared with back-scattered images. This scattering asymmetry is typical of particles with sizes on the order of a micron or less. Particles of this size have destruction and orbital evolution lifetimes of 10^5 years or less, so sources to replenish the dust are required (Burns et al., 2004). The gossamer ring systems may be populated by the inward evolution of ejecta from micrometeorite impacts on Thebe and Amalthea, as suggested by the structure of these systems (de Pater et al., 1999; Ockert-Bell et al., 1999; Burns et al., 1999). The observed structure of the halo (de Pater et al., 1999; Ockert-Bell et al., 1999) implies the inward orbital evolution of small, charged dust particles whose inclinations are excited at Lorentz resonances (Schaffer and Burns, 1992; Hamilton, 1994; Horányi and Cravens, 1996). In the main ring, as in the gossamer ring, dust is thought to be generated via micrometeorite impacts on parent bodies, whose collective cross section is estimated to be about three times that of Metis and Adrastea combined, based on Galileo imaging data (Burns et al., 2004).

The observations reported here were conducted in 2002 and 2003 with the 10-m telescopes at the W.M. Keck Observatory during the 2002 jovian ring plane crossing. We present a near-infrared spectrum covering the 2.2–3.0 μm range, supplemented with imaging photometry taken with a CH4-band (2.27 μm) filter and a narrowband FeII filter (1.64 μm), and with adaptive optics images taken in the L´ band spanning 3.5–4.1 μm. We also include data from two 1997 ring plane crossing CH4-band images, one of which was previously published in de Pater et al. (1999). Galileo NIMS spectra of the ring in forward-scattered light between 0.7–5.2 μm (McMuldroch et al., 2000; Brooks et al., 2004) overlap with our data in the spectral domain, but the difference in phase angle means that the Keck and NIMS data sets are sensitive to different particle characteristics. The NIMS data were able to strongly constrain the fine dust grain sizes, while the ground-based data are sensitive to the larger ring particles in addition to the fine dust. Our data add to a body of discrete measurements of the ring's near-infrared reflectivity in back-scattered sunlight (e.g., Neugebauer et al., 1981; Meier et al., 1999; de Pater et al., 1999; Nicholson and Matthews, 1991; Brown et al., 2003), yielding some insight into the composition of the larger particles in the ring system.

2. Observations

Images and spectra of Jupiter's ring were obtained near the 2002 ring plane crossing. The ring opening angle for 2002 and 2003 observations was 0.04°. Table 1 lists the detailed geometry of the observations.

2.1. Images

We imaged Jupiter's ring with the facility's near-infrared camera NIRC (Matthews and Soifer, 1994) on 19 and 21 December 2002 (Table 1), using the CH4 (Fig. 1) and FeII (Fig. 2) filters, respectively. NIRC is equipped with a 256 × 256 pixel Santa Barbara Research Corporation InSb array, and has pixel size of 0.151″. The seeing on 19 December was 0.77″, estimated from the width of the main ring itself in the CH4 data set. For the FeII data on 21 December, we estimated the seeing to be 0.73″ based on the width of the main ring in the co-added data or 0.62″ based on individual calibration star frames. We

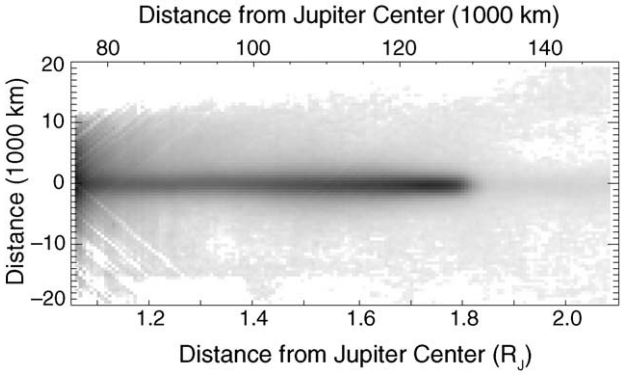

Fig. 1. Co-added NIRC image of the main ring and halo, taken with the CH4 filter (see Table 1) in 2002. This image was used for absolute calibration of the NIRSPEC spectral data.

Table 1
Summary of ring observations

Date	Instrument	Filter	λ_{min} (μm)	λ_{min} (μm)	Range (AU)	Solar distance (AU)	Phase angle	Pixel size (″/pix)	Pixel size (km/pix)	T_{int} (s)
1997-08-14, 15	NIRC	CH4	2.191	2.346	4.053	5.0611	1.2°	0.151	444	5300[a]
1997-10-22	NIRC	CH4	2.191	2.346	4.714	5.0406	11.0°	0.151	516	3200[a]
2002-12-19	NIRC	CH4	2.191	2.346	4.614	5.2978	8.22°	0.151	505	5580[a]
2002-12-21	NIRSPEC	KL[b]	2.20	3.03	4.590	5.2985	7.94°	0.116[c]	386	1080
2002-12-21	NIRSPEC	KL[b]	2.83	3.65	4.590	5.2985	7.94°	0.116[c]	386	550
2002-12-21	NIRC	FeII	1.6383	1.6559	4.613	5.2985	7.94°	0.151	505	360
2003-01-22	NIRC	CH4	2.191	2.346	4.345	5.3090	2.3°	0.151	476	1760[a]
2003-01-26	NIRC2/AO	L´	3.426	4.126	4.334	5.3103	1.51°	0.01	31.4	648

[a] NIRC CH4-band image times are given for the total time spent on entire ring system.
[b] NIRSPEC wavelength range set by the grating cross-disperser position is narrower than that of the filter.
[c] NIRSPEC pixel scale after rectification (see text); raw data scale is 0.143″/pixel. SCAM resolution is 0.18″/pixel.

Please cite this article as: M.H. Wong et al., Ground-based near infrared spectroscopy of Jupiter's ring and moons, Icarus (2006), doi:10.1016/j.icarus.2006.07.007

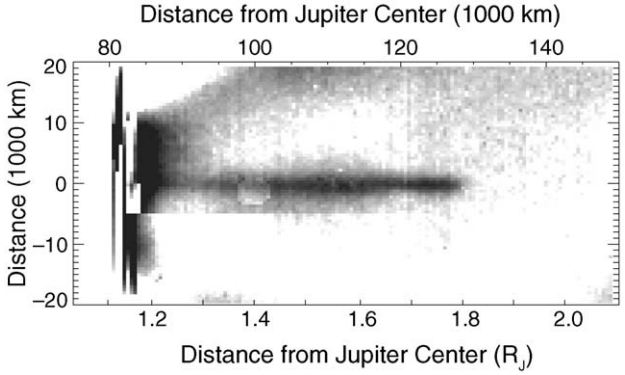

Fig. 2. Co-added NIRC image of the main ring and halo, taken with the FeII filter (see Table 1) in 2002. Satellite subtraction has left a circular artifact near 1.4 R_J; the brightness discontinuity 5000 km below the ring plane is due to missing data in some of the individual frames.

linearized and flat-fielded the data according to standard procedures (Graham et al., 1994). Separate sky frames were acquired and subtracted from the ring images (see procedures described by de Pater et al., 1999). Bleeding to adjacent pixels was corrected according to an empirical model based upon observations of stars (Liu, 2000; Liu and Graham, 2001), and stray light from Jupiter was removed by modeling the background based on scans above and below the ring's halo. The absolute calibration of the images was set by observing the infrared standard stars SJ9134 and SJ9138 (Persson et al., 1998). In this paper we are primarily concerned with Jupiter's main ring and halo, and in particular with its flux density; our CH4 imaging data have excellent information regarding the gossamer rings, which will be described in a separate report (Showalter et al., 2006).

Values of the reflectivity, I/F, were calculated using library solar spectra of Colina et al. (1996) at $\lambda < 2.5$ μm and of Labs and Neckel (1968, 1970) longward of 2.5 μm. We define the ratio of the ring flux density I to the incident solar flux density πF at Jupiter's ring (following the typical convention of, e.g., Hammel et al., 1989):

$$\frac{I}{R} = \frac{R^2}{\Omega}\frac{f_\lambda}{F_E},$$

where R is Jupiter's heliocentric distance (in AU), is the observed solid angle corresponding to the observed flux f_λ, and πF_E is the solar flux at 1 AU. The units of f_λ and F_E are the same; in this case we measure the flux density in Jy. Integrating the I/F (Nicholson et al., 1996) with respect to projected image distance perpendicular to the ring (in meters) yields a quantity with a slightly more intuitive physical interpretation: the vertically integrated I/F (VIF). The VIF gives an idea of the amount of ring material present in the line of sight, since it is equivalent to the thickness (perpendicular to the ring plane) of a solid ring with $I/F = 1$.

Imaging Jupiter's ring from Earth at L´-band (3.5 μm) has been unsuccessful to date. Because the main ring is unresolved perpendicular to the ring plane, the signal-to-noise ratio improves with increasing resolution. Thus, we observed Jupiter's ring plane with adaptive optics on 26 January 2003, using the

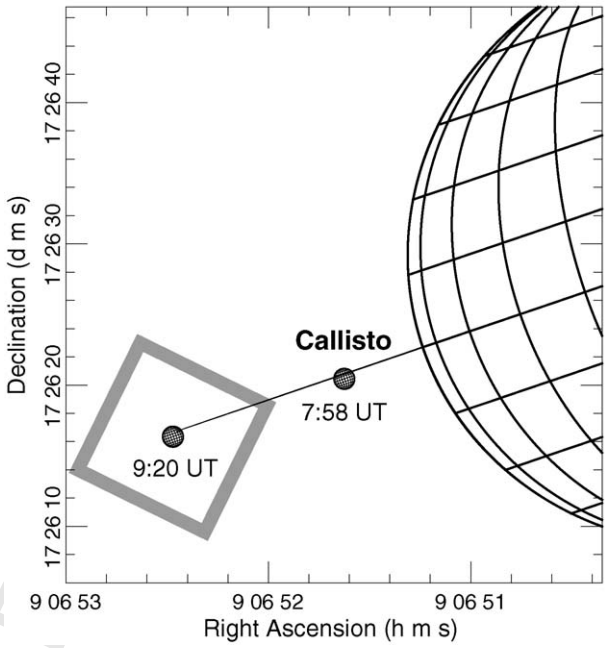

Fig. 3. The NIRC2 AO frames in the L´ band were acquired as Callisto moved outwards through the ring plane, starting at 7:58 UT and ending at 9:20 UT. The grey box shows the field of view and orientation of the NIRC2 camera (map generated by the PDS Planetary Rings Node Jupiter viewer at http://pds-rings.seti.org).

Satellite Callisto for wavefront sensing. The L´ observations were conducted between 7:58 and 9:20 UTC, during which time Callisto moved outwards along the ring plane as indicated in Fig. 3. Standard near-infrared data reduction techniques (flat-fielding, sky subtraction, bad pixel replacement with the median of surrounding pixel values) were applied to the images. Absolute calibration was performed on stars HD106965 and HD22686 (Elias et al., 1982). Fig. 4 shows an image constructed by co-adding frames aligned on Callisto; had the ring been detected, it would have run horizontally through Callisto in the image.

Although we could not detect the ring in our co-added L´ data, we are able to determine a robust upper limit for the I/F of the ring in L´-band from the data. To reduce noise, we averaged pixels within rows of the image, resulting in a vertical trace that cut through the position of the ring plane. We subtracted a linear background near the expected ring position, and estimated the 1-σ root-mean-square noise level of the trace to be equivalent to 0.81 m VIF. Unfortunately, we cannot claim 0.81 m (or 2.4 m for 3-σ) for the upper limit, because the ring's flux is spread by the telescope optics over several pixels, not isolated to a single pixel row. We observed a star to measure the point spread function (PSF) of the telescope. The correct way to estimate the ring upper limit is then to integrate over the whole PSF, after scaling the PSF so that its peak (central) intensity is equal to the desired 1-σ noise level in the data as described above. This method yields a 1-σ upper limit for the ring of 11 m VIF, although examination of the data reveals that the 2-σ value of 22 m VIF is a more realistic detection limit.

Please cite this article as: M.H. Wong et al., Ground-based near infrared spectroscopy of Jupiter's ring and moons, Icarus (2006), doi:10.1016/j.icarus.2006.07.007

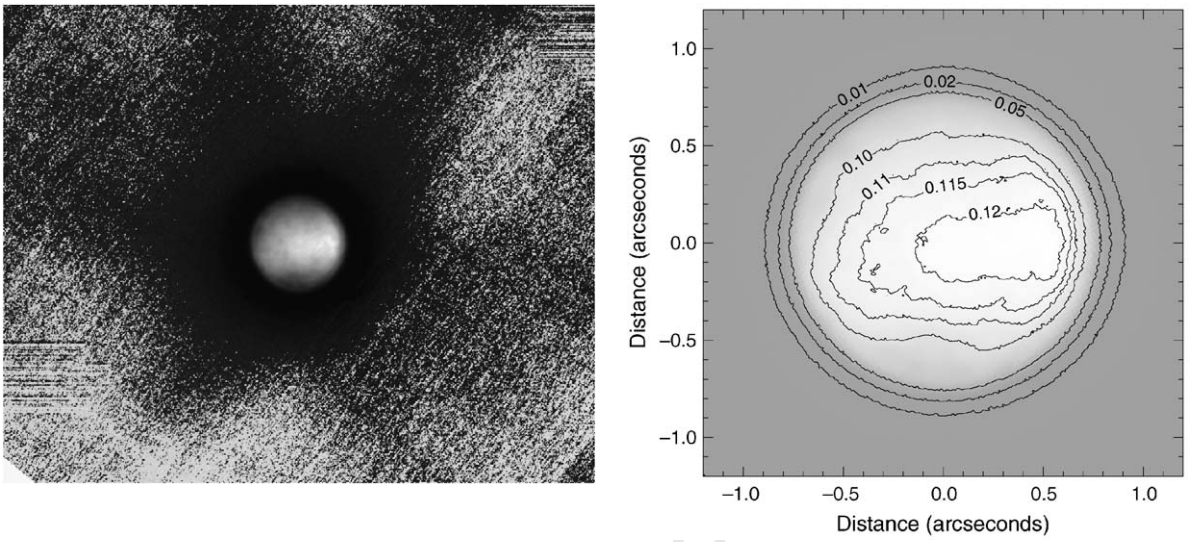

Fig. 4. Sum of several NIRC2 AO frames in the L′ band, aligned on Callisto (see Table 1). Images are oriented so that the ring plane is along the horizontal axis. Left: The background has been inverted and stretched for clarity. If the ring were detectable, it would appear as a very thin horizontal line centered on Callisto, which was moving through the ring plane while these frames were acquired. The hexagonal pattern in Callisto's stray light background is due to telescope optics. Right: Contours show Callisto I/F values. The leading hemisphere (left) is slightly darker than the trailing hemisphere. During the time of the observations, Callisto's sub-Earth longitude ranged from 1.4° to 2.6°, and the sub-Earth latitude remained fixed at 0.04° S.

2.2. Spectra

The spectra were obtained with the near-infrared spectrometer NIRSPEC (McLean et al., 1998) in the low resolution mode ($R \sim 2000$), using the KL filter. The spectrograph slit width was 0.76″, with a length of 42″, and the slit was aligned parallel to the ring plane. NIRSPEC is equipped with a 1024 × 1024 InSb array for spectroscopy and a slit-viewing camera (SCAM), which consists of a 256 × 256 HgCdTe array of 0.18″ pixels, yielding a field of view 46″ square. We used grating cross-disperser position of 31.14 to observe the 2.20–3.03 μm (Table 2) spectral interval. Fig. 5 shows the geometry of the observations. The slit was alternately placed along the ring plane to integrate on the ring, and offset from the ring plane (pictured) to obtain background sky frames. Since satellites had to be masked out of some frames, the total integration times reported in Table 1 are upper limits; the actual integration time for some parts of the data set are reduced by the integration time of one or more frames. Individual frames in the 2.20–3.03 μm data set had integration times of 60 s. Unfortunately, as is discussed below, the ring was not detectable in the data longward of about 2.5 μm. Additional data sets at 2.83–3.65 μm using the KL filter with the cross-disperser position set to 32.63, at 0.95–1.12 μm with the NIRSPEC-1 filter, at 1.6–2.0 μm with the NIRSPEC-6 filter, and at 1.95–2.29 μm with the K' filter also could not detect the ring above the background of stray light from Jupiter. To perform spatial rectification and to obtain the wavelength solution for the NIRSPEC data, we used spectra of argon calibration lamps and the REDSPEC v2.5 package of IDL routines.[1] The nominal NIRSPEC plate scale in the spatial direction (along the spectrograph slit) is 0.143 arcsec pixel^{-1} in the raw data (McLean et al., 1998). For the rectified data, we derived a plate scale of 0.116 arcsec pixel^{-1} by comparing the observed and ephemeris-predicted positions of Amalthea in 13 frames (listed in Table 2). The co-added ring spectrograph image was composed of frames aligned on Jupiter's limb (as determined at four wavelengths), since the ring is too faint in individual frames to use for alignment.

Sky frame subtraction was used to reduce four competing sources of noise: detector bias and dark current, sky emission, stray light in the spectrograph, and stray light near the disk of Jupiter. For on-ring frames, the "Sky Frame" column in Table 2 gives the name of the sky frame subtracted from the data. We built sky frames A–E by co-adding groups of off-ring frames with similar jovian limb placements; the individual co-added frames used for each sky frame can be read from Table 2 as well. We found that due to the very low flux density from the ring, it was necessary to first subtract sky background frames before shifting and adding frames. Detector effects and stray light in the spectrograph are best eliminated by subtracting unshifted frames, because the stray light in the spectrograph is strongest at the ends of the slit (corresponding to the data both on the disk and farthest from Jupiter) but is relatively constant away from these extremes. On the other hand, stray light from Jupiter is ideally removed by subtracting sky frames after limb-aligning them with the ring frames, but we achieved satisfactory results by choosing sky frames whose unshifted limb positions differed by less than 17 pixels (2″) from the corresponding ring frame limb positions. The best compensation for sky emission would have been achieved by subtracting sky frames that were acquired the closest (in time) to the corresponding ring frames, but this sort of temporal pairing would have interfered with the limb-proximity pairing used to correct for scattered light from the jovian disk. The combination of

[1] REDSPEC was developed by S.S. Kim, L. Prato, and I.S. McLean at the UCLA Astronomy department. REDSPEC is available from the Keck website and was created to supported NIRSPEC data analysis.

Table 2
NIRSPEC 2.2–3 μm observation details

Frame	Time (UTC)	Slit on ring	Sky frame	Position in frame (pixel row No.)		Amalthea offset from Jupiter center	
				Limb	Amalthea	(arcsec)	(R_J)
1169	14:32:56	x	B	282.56	88.11	42.97	2.00
1170	14:34:26		A	290.02	–	–	–
1171	14:37:01	x	C	275.14	90.82	41.74	1.95
1172	14:38:37		B	283.49	–	–	–
1173	14:40:02		B	286.47	–	–	–
1174	14:42:18	x	C	272.20	101.62	40.07	1.87
1175	14:43:51	x	C	271.61	105.70	39.57	1.84
1176	14:45:18	x	C	274.08	111.66	39.09	1.82
1177	14:46:56		B	283.13	–	–	–
1178	14:48:20		C	280.36	–	–	–
1179	14:49:47		C	279.25	–	–	–
1180	14:51:09		C	279.69	–	–	–
1181	14:53:32	x	C	270.73	134.32	36.26	1.69
1182	14:55:02	x	C	272.49	137.91	35.72	1.67
1183	14:56:26	x	C	270.61	140.52	35.21	1.64
1184	14:57:51	x	D	263.79	138.22	34.69	1.62
1185	14:59:17	x	D	257.03	137.72	34.16	1.59
1186	15:01:02		D	258.61	–	–	–
1192	15:09:50		E	310.96	–	–	–
1193	15:11:28	x	A	287.78	209.23	29.45	1.37
1194	15:12:50	x	B	282.55	208.12	28.90	1.35
1195	15:14:24	x	A	289.52	222.73	28.27	1.32
1196	15:15:49	x	B	281.19	218.30[a]	27.60[a]	1.29[a]
1197	15:17:12	x	C	273.43	224.35[a]	27.00[a]	1.26[a]
1198	15:18:35	x	C	268.32	215.01[a]	26.49[a]	1.23[a]
1202	15:26:35	x	E	305.19	281.11[a]	23.10[a]	1.08[a]
1203	15:28:05	x	E	298.91	280.03[a]	22.50[a]	1.05[a]
1204	15:29:27	x	E	293.19	280.34[a]	21.80[a]	1.02[a]

[a] After 15:15 UT Amalthea was in eclipse and could not be detected in the data.

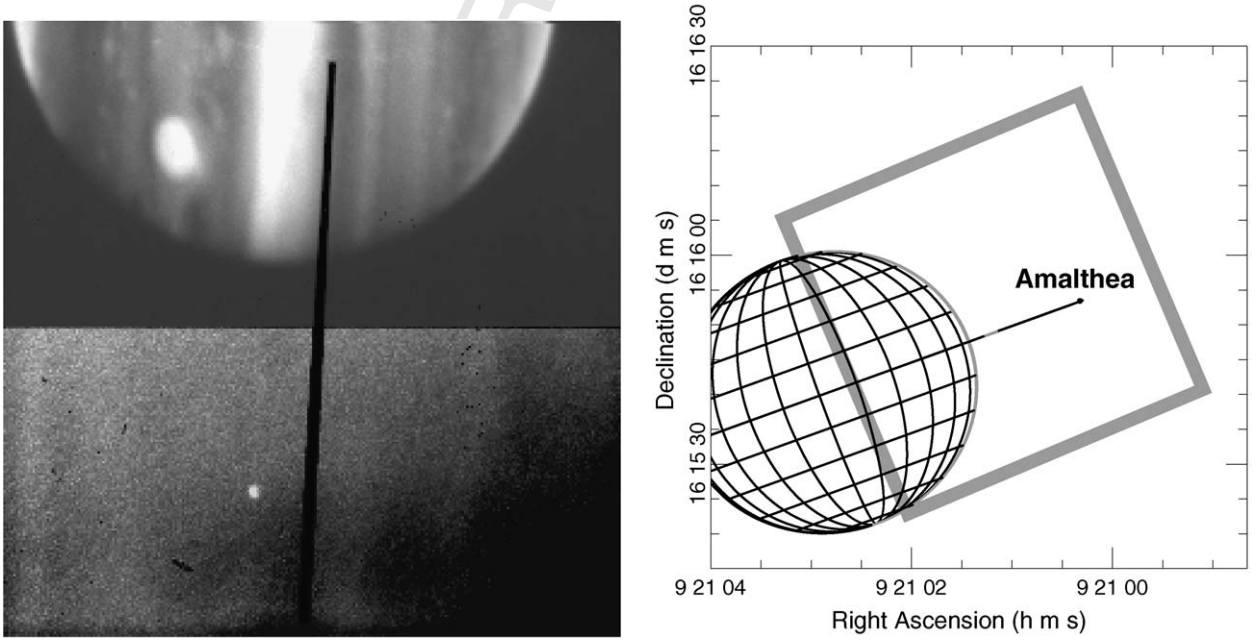

Fig. 5. An image from the slit-viewing camera (SCAM) taken at 14:48 UT on 2002-12-21 (left) shows the NIRSPEC slit offset from Jupiter's equatorial plane during one of the background exposures. Two image contrast scales are used to show both Jupiter and Amalthea; the main ring is barely visible in this 10-s exposure. The geometry of Jupiter, the main ring, and Amalthea is shown on the right, with the SCAM field of view denoted by the grey box, rotated so that the slit is parallel to the ring plane (map generated by the PDS Planetary Rings Node Jupiter viewer at http://pds-rings.seti.org).

Please cite this article as: M.H. Wong et al., Ground-based near infrared spectroscopy of Jupiter's ring and moons, Icarus (2006), doi:10.1016/j.icarus.2006.07.007

increasing sky emission and decreasing solar intensity with increasing wavelength meant that the ring spectrum could not be retrieved from this data set for wavelengths longer than 2.5 μm. In retrospect, since the low intensity of the ring necessitated accurate corrections for numerous background contributions, the best observing strategy would have been to obtain images with the limb at the same position in every frame (both on and off the ring plane), with more frequent interleaving of sky and ring frames. We observed the A1V star HIP 45874 in order to correct for atmospheric extinction. All spectra were divided by the average spectrum of this calibration star, and then multiplied by a blackbody spectrum at 9325 K.

A background bias correction was applied to the processed data (after co-adding, sky-subtraction, extinction–correction, and limb-alignment) by subtracting the average level just beyond the main ring (1.83 to 1.95 R_J) at each wavelength. The bias correction is thus most accurate near the ring ansa, with declining accuracy closer to the planet. The bias-correction technique also cancels the 2.7% contribution from the gossamer rings (de Pater et al., 1999).

Stray light from Jupiter is removed from the data by subtracting off-ring frames with the limb of Jupiter falling at approximately the same pixel row as in the on-ring frames, but some residual stray light remains even after this step. Stray light increases dramatically longward of about 2.46 μm as Jupiter's methane band is left behind and Jupiter grows much brighter. Visual inspection of these data outside the methane band shows strong stray light effects out to 1.6 R_J from the planet, but we estimate (based on the ring data itself) that the stray light limiting distance within the methane band is at a more favorable 1.45 R_J.

We "bootstrapped" the 2.20–2.47 μm ring spectrum absolute flux calibration using the calibrated NIRC image (Fig. 1; Table 1) taken with the CH4 filter ($\lambda_{central} = 2.269$ μm; full width at half maximum = 0.155 μm). Explicitly, we summed the CH4 image intensity over a rectangular solid angle spanning 1.6–1.8 R_J in the radial direction (covering the ring ansa) and 0.763″ perpendicular to the ring plane (corresponding to the projected linear width at Jupiter of the NIRSPEC spectrograph slit). The resulting flux density from the image was 710 μJy. We then scaled the NIRSPEC flux density so that the total flux density within the wavelength interval of the CH4 image and between 1.6 and 1.8 R_J was also 710 μJy.

3. Results and discussion

3.1. Ring imaging

3.1.1. Solar phase angle dependence (CH4 filter)

We have extracted thin radial profiles to focus on the main ring and thick profiles to include the halo (see Fig. 6). We chose profile widths following de Pater et al. (1999), with thin profiles vertically integrated over 2210 km (or about 0.031 R_J, corresponding to the 0.75″-wide profiles shown in de Pater et al., 1999), and with thick profiles spanning 17,350 km perpendicular to the ring plane, or about 0.243 R_J (corresponding to the 5.9″-wide profiles shown in de Pater et al., 1999). In addition

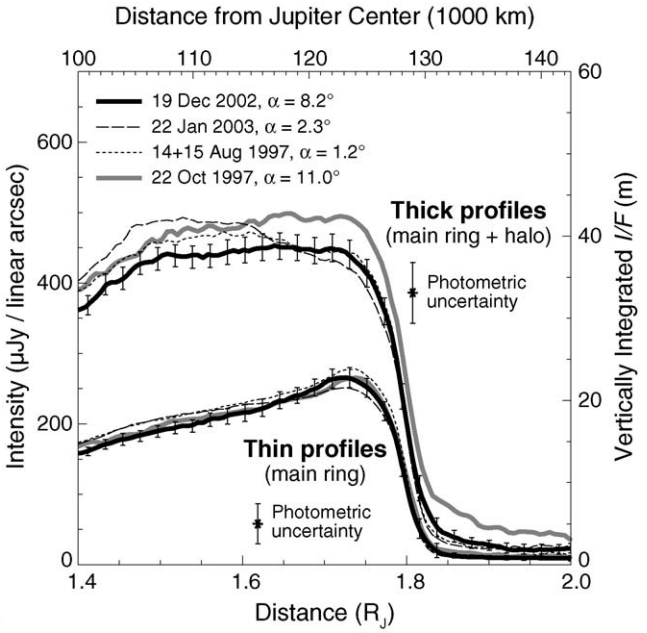

Fig. 6. Radial profiles from NIRC CH4-band images obtained at four epochs with different phase angles (see legend). There are no differences in brightness or shape among the thick and thin profiles that are clearly above the 1-σ uncertainty level, so the phase response of the main ring and halo is quite flat over the 1.2°–11° phase angle range. Intensities are given in μJy/linear arcsec along the ring plane, integrated over 0.75″ (thin profiles) and over 5.9″ (thick profiles). Error bars shown for the December 2002 data indicate the 1-σ noise level common to all the profiles after smoothing by three pixels (equivalent to 0.014 R_J, or the distance between two error bars), and the photometric uncertainty is shown separately for the thin and the thick profiles. The photometric uncertainty is larger for the thick profiles than for the thin profiles because it scales with intensity. Flux density values and profile angular thicknesses have been scaled to match the August 1997 geocentric and heliocentric distances.

to radial profiles extracted from the December 2002 CH4-band image, Fig. 6 also shows profiles extracted from NIRC CH4-band images acquired in August 1997 (de Pater et al., 1999), October 1997, and January 2003. The thin profiles are identical to within the stated uncertainties. The thick profiles also do not show any variation in peak intensity greater than the photometric uncertainty. Although the thick profiles do exhibit some variation in shape at the 1-σ level, the statistical significance of this variation is dubious.

The CH4-band data are plotted vs phase angle in Fig. 7. Each point is a radial average of the profiles shown in Fig. 6, with open squares corresponding to the thick profiles and filled squares corresponding to the thin profiles. Both thick and thin profiles are best fit by straight lines, indicating reflectivities independent of phase angle to within the 1-σ error-bars. The solid curve shows the model phase function of Throop et al. (2004), which was scaled to best fit the data. The Throop et al. (2004) phase function is consistent with the data at the 1-σ level, but does not provide a better fit than a straight line. The model phase function includes contributions from both the fine dust and the large ring particle components. The fine dust component was modeled using the Mishchenko and Travis (1998) code for non-spherical scattering and absorption, using the size, shape, and composition parameters from Throop et al. (2004).

Please cite this article as: M.H. Wong et al., Ground-based near infrared spectroscopy of Jupiter's ring and moons, Icarus (2006), doi:10.1016/j.icarus.2006.07.007

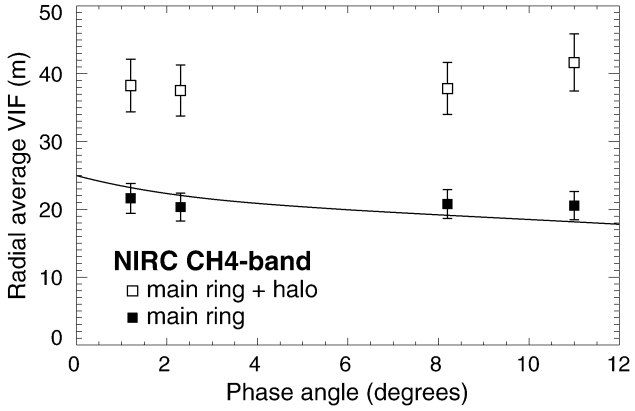

Fig. 7. Main ring and halo phase function from CH4-band imaging data. The profiles in Fig. 6 were radially averaged over the 115,000 km to 125,000 km interval, and these mean values are plotted here as a function of phase angle. The phase function produced with best fit parameters from Throop et al. (2004) is shown as a solid line; it is marginally consistent with the CH4-band phase function at the 1-σ level. The opposition peak ($\alpha < 2°$) in the model is due to the choice of Callisto cratered terrain (Squyres and Veverka, 1981) as an analogue for the phase function of large bodies in the main ring, so the relative lack of opposition surge in the observations themselves may signal a lack of regolith material on the larger ring bodies.

The large particle component was modeled using the Callisto phase curve of Squyres and Veverka (1981), again following Throop et al. (2004).

Since the ratio of large particle to dust optical depths, τ_l/τ_s, found by Throop et al. (2004) is 3.6 for non-spherical particles, the large particle contribution dominates at the small phase angles sampled by our ground-based measurements. The Squyres and Veverka (1981) phase function was originally derived simply as an empirical fit to Callisto phase function data taken by Voyager, but it models a clear opposition surge. Throop et al. (2004) found a very good fit to jovian ring data using this phase function to model the behavior of the large ring particles at larger phase angles, but this phase curve produces a slope that is barely consistent (at the 1-σ level) with our ring data at smaller phase angles. In fact, a phase-invariant reflectance over the 1.8°–11° range sampled by the data fits better than the Squyres and Veverka (1981) formulation. The angular width of the opposition surge on a body is linked to physical properties of the regolith on the body's surface (Hapke, 1986), so the lack of a clearly detectable opposition surge in our data may indicate an absence of regolith on ring parent bodies. The lack of a regolith is not surprising, since the location of these objects within Jupiter's Roche limit would make the retention of a regolith difficult. In addition, the role of parent bodies as replenishers of the dust component of the ring implies that dust created by micrometeorite impacts or collisions would be efficiently lost to the ring, rather than remaining on the surface of the parent bodies. The flat phase curve in the data parallels recent work by Showalter et al. (2006) showing that the jovian gossamer rings also have no phase angle dependence near backscatter. Showalter et al. (**?**) attribute this uniformity to non-spherical gossamer ring dust particle shapes. Our results suggest that main ring dust may also be non-spherical, and that

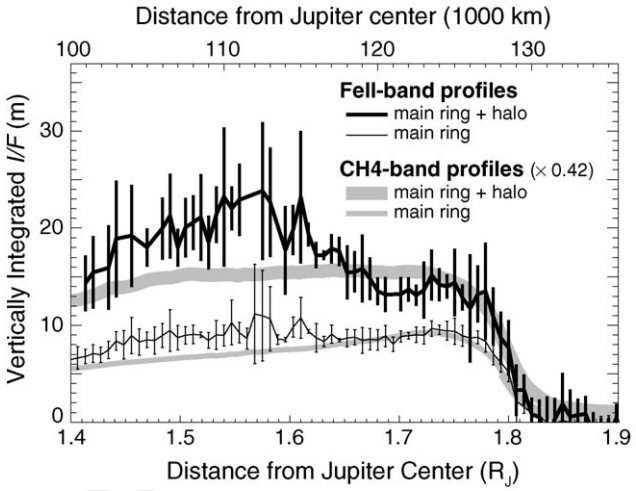

Fig. 8. Radial profiles of ring system reflectivity obtained from the FeII image (Fig. 2). The main ring profile (thin black line) is integrated over a 2200-km swath centered on the ring plane, and the main ring + halo profile (thick black line) shows the "total" ring system reflectivity summed over 17,300 km centered on the ring plane. The drop in reflectivity out to 1.67 R_J in the thick profile is due to the halo. CH4-band profiles from Fig. 6 (scaled by 0.42) are shown in grey for comparison. The plotted error bars show statistical uncertainties estimated using standard deviations from the individual frames used to make the co-added image shown in Fig. 2.

ring parent bodies may lack regoliths. Model fits to Cassini, Galileo, and Voyager visible phase curve data also strongly require non-spherical main ring dust particles (Porco et al., 2003; Throop et al., 2004).

3.1.2. *Halo imaging (CH4 and FeII filters)*

Fig. 8 shows thick and thin profiles derived from the FeII image. Between 1.7 and 1.8 R_J, there is a minimal difference (about 4 m VIF) between the thin strip and the thick strip. This result is expected, given the fact that the ring is unresolved; the projected width of 2074 km corresponding to the 0.62″ seeing estimated from calibration star images is much greater than the 57-km thickness due to the combination of the projected ellipse of the ring with an opening angle of 0.04° and the physical thickness in backscattered light determined from Voyager data (Showalter et al., 1987). The VIF in the thick (main ring + halo) profile is roughly constant over the 1.45 to 1.6 R_J region at about 20 m and decreases over the outer range of the halo at 1.6 to 1.7 R_J. To assess the spatial distribution of the halo in the FeII image, we show the width of the ring as a function of distance in Fig. 9. We calculated the width by fitting each column of the co-added image with a linear background and a Gaussian, so the full width at half maximum of the fitted Gaussian is the quantity plotted in Fig. 9. Horizontal lines contrast the average width of the ring interior to 1.6 R_J ($1.18 \pm 0.04''$ or 3950 ± 130 km) as well as over the 1.7–1.8 R_J region ($0.75 \pm 0.03''$ or 2510 ± 100 km).

Grey curves in Fig. 8 enable comparison of the CH4 profiles (scaled down by a factor of 0.42) with the FeII profiles. The factor of 0.42 basically turns down the brightness of the main ring (1.7–1.8 R_J) at the CH4-band wavelength of 2.27 μm, to

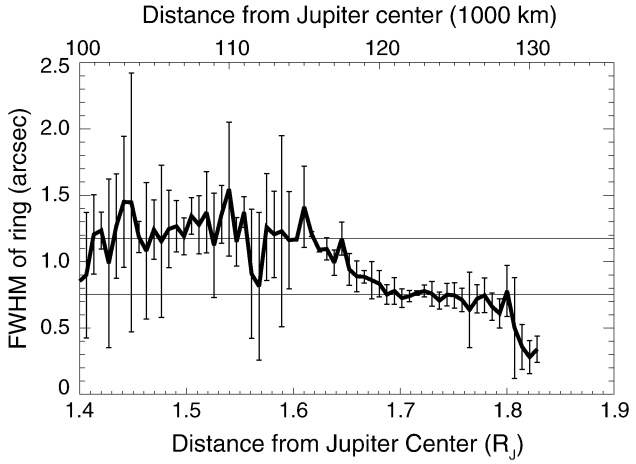

Fig. 9. Ring system width. For each column in the FeII image (Fig. 2), a Gaussian + linear background fit was made to the data. The full width at half maximum of the fitted Gaussian (thick curve) drops from the average value of $1.18 \pm 0.04''$ inward of 1.6 R_J (where the halo contributes to the ring system reflectivity) to $0.75 \pm 0.03''$ over the 1.7–1.8 R_J region. The scale is 3329 km/arcsec, but the edge-on main ring itself is unresolved (perpendicular to the ring plane).

match the main ring brightness at the FeII-band wavelength of 1.64 μm. The clear excess in FeII over CH4 inside of 1.6 R_J, due to the halo contribution, shows that the halo is not as red as the main ring. The relative magnitude of the halo contribution (the difference between the thick and thin profiles) is also greater in the FeII band than in the CH4 band, again consistent with a redder color of the main ring with respect to the halo. Since the main ring's backscattered reflectance is about evenly divided between solid bodies and dust, while the halo reflectance is entirely due to dust, this observed halo-main ring color difference is probably caused by the previously known intrinsically red color of the large bodies of the main ring. But unfortunately, stray light from the jovian disk is also at least an order of magnitude brighter in the FeII band (based on spectra presented by Banfield et al., 1998), and could influence the results despite our best attempts to correct for instrumentally scattered Jupiter light. Reflected Jupiter shine—sunlight scattered from Jupiter to the halo and back to the observer—may play a significant role just because Jupiter occupies such a large solid angle as seen from the halo. For a ring or halo particle, the situation is analogous to the bright glare experienced by a snowboarder on a sunny day: although the Sun is indeed brighter than a similarly sized patch of snow, the large areal extent of the snowfield makes it a strong local source of illumination. This effect approximately follows an inverse r^2 dependence over the 1.4–2.0 R_J range. At the halo's distance of 1.6 R_J, Jupiter shine is 30% stronger than at the main ring's distance of about 1.8 R_J, not only in our data, but in any remote sensing data set. Thus it is not entirely clear whether we have detected a true color difference between the ring and the halo, or whether we are seeing more scattered Jupiter shine from the halo than from the main ring.

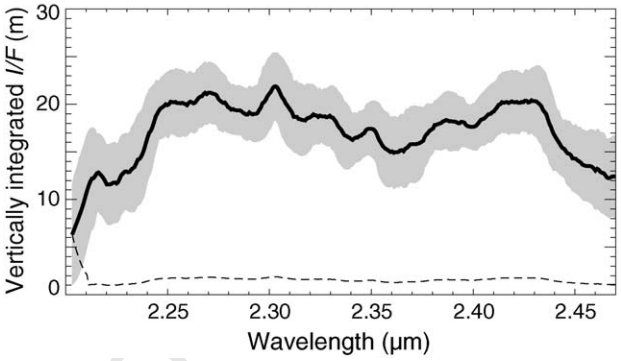

Fig. 10. Main ring spectrum from 2.2–2.5 μm, averaged over 1.6–1.8 R_J. Individual data points are averaged from co-added spectra and Gaussian smoothed with a half width of 5.4 nm, from low-resolution NIRSPEC data with an original $\Delta\lambda$ of 0.8 nm. The grey error-band shows the 1-σ statistical uncertainty envelope for the smoothed data, while systematic uncertainties are plotted as a dashed line.

3.2. Ring spectroscopy

3.2.1. NIRSPEC spectrum (2.2–2.5 μm)

The spectrum of the ring between 2.20 and 2.47 μm is shown in Fig. 10, averaged over data with projected jovian separations of 1.6 to 1.8 R_J. Examination of the data revealed no significant difference between the spectral character of the ring system observed at the main ring ansa (1.6–1.8 R_J; shown in Fig. 10) and closer to the planet, where the halo contribution is larger (1.45–1.6 R_J; not shown).

Fig. 11 (adapted from Throop et al., 2004) expands the wavelength scale to show the NIRSPEC main ring spectrum in comparison to adjacent 2–2.5-μm measurements (from Meier et al., 1999; Neugebauer et al., 1981; Nicholson and Matthews, 1991, adjusted to compensate for viewing geometry according to Throop et al., 2004). The main ring spectrum is consistent with these other results, except for the Neugebauer et al. (1981) measurements at 2.2 and 2.4 μm. The Neugebauer et al. (1981) data, including the point at 1.7 μm, differ from the other measurements in Fig. 11b in that they used a relatively large 6″ photometric aperture, which would have included additional flux from the halo. The other data sets used imaging photometry, with the wavelength range of the observations represented using horizontal error bars in Fig. 11b.

The ring spectrum is flat over the 2.25 to 2.45 μm interval, with a possible absorption feature shortward of 2.25 μm. No previous measurements had narrow enough spectral bandwidths to detect a feature at this wavelength. Based upon the KL filter transmission spectrum, this feature does not appear to be an artifact. It is also hard to explain as being caused by Jupiter stray light. If stray light were to account for the observed spectral feature somehow, we would expect a continuous effect over the 2.2–2.3 μm region. In particular, the flat spectrum between 2.25 and 2.30 μm is difficult to explain via variations in stray light intensity, since Jupiter is about a factor of three brighter at 2.25 μm than at 2.30 μm (Banfield et al., 1998). Furthermore, examination of Amalthea spectra, even at separations as small as 1.32 R_J showed no anomalous effect on the slope of the Amalthea spectrum due to stray light at $\lambda < 2.3$ μm. However,

Please cite this article as: M.H. Wong et al., Ground-based near infrared spectroscopy of Jupiter's ring and moons, Icarus (2006), doi:10.1016/j.icarus.2006.07.007

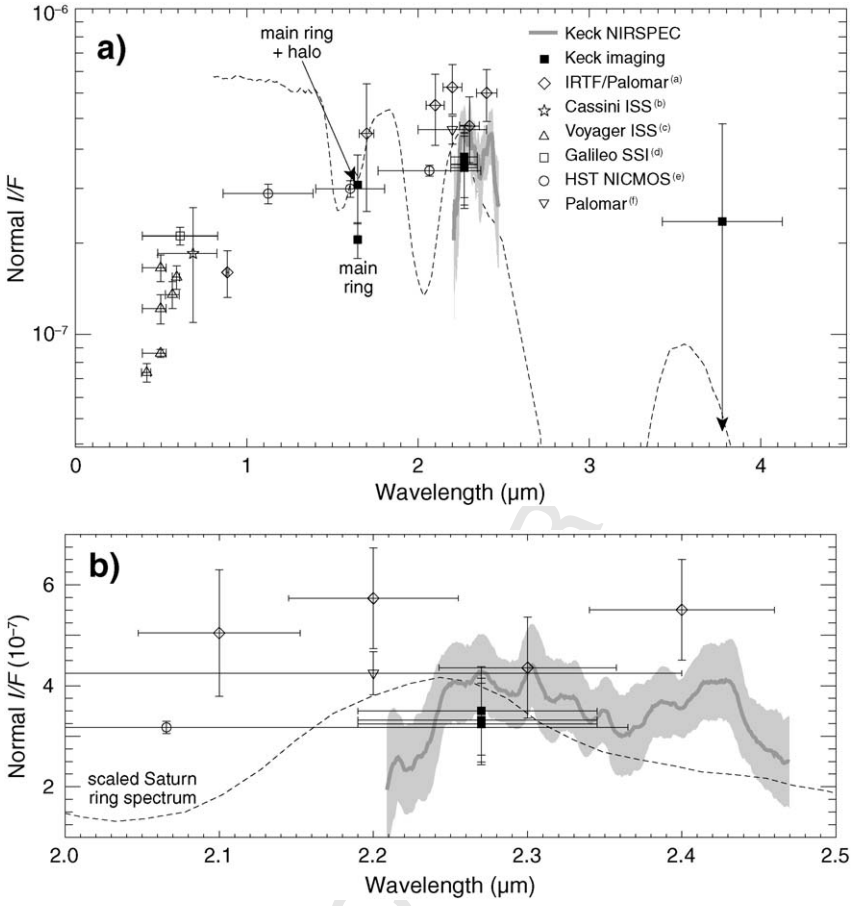

Fig. 11. Spectral measurements of the backscattered main ring reflectivity, after corrections for variance in the viewing geometry from data set to data set (adapted from Throop et al., 2004). Horizontal bars indicate the wavelength span of each measurement. The NIRSPEC data are shown as a dark grey curve, with the uncertainties represented as a light grey error envelope. The Keck data points at 1.64 μm show the difference in normal reflectance derived when the halo is included in the measured ring reflectance. The Keck data point near 3.8 μm is the 1-σ upper limit obtained from our L´-band image, with the 2-σ upper limit also indicated as the upper error bar. The Keck data points near 2.27 μm at phase angles of 1.2°, 2.3°, 8.2°, and 11° are identical within the error estimates (see Fig. 6 and Table 1). The individual observations are described in Throop et al. (2004) and (a) Neugebauer et al. (1981), (b) Throop et al. (2004), (c) Showalter et al. (1987), (d) Ockert-Bell et al. (1999), (e) Meier et al. (1999), (f) Nicholson and Matthews (1991).

the usefulness of Amalthea's spectrum as a diagnostic is limited for two reasons: Amalthea's greater brightness relative to the ring means that (instrumental) stray Jupiter light should influence the satellite's spectrum much less than the ring's spectrum, and the ring's separation of only 0.8 R_J from Jupiter would make (non-instrumental) scattered Jupiter shine about 2 times weaker for Amalthea than for the main ring.

The possible absorption band in the NIRSPEC data shortward of 2.25 μm may be consistent with Cassini VIMS phase data. Model phase curves of Throop et al. (2004) found a better match to the 60°–120° VIMS data using only dust, rather than a combination of dust and large ring bodies. This implies that the large bodies are anomalously dark in the wavelength range sampled by the VIMS data. Throop et al. (2004) invoked the possibility that the feature could be similar to 2-μm pyroxene/olivine bands seen in asteroids (Bell et al., 1988; Gaffey et al., 1993). Alternately, the 2-μm water ice feature (Warren, 1984; Rajaram et al., 2001; Gerakines et al., 2005) would be an unconventional suggestion, given substantial work showing that water ice is unstable to sputtering over short time scales in the jovian ring system. Morfill et al. (1980) and Burns et al. (1984) showed that icy dust grains would be destroyed by sputtering on the order of 100 times faster than silicate grains. Johnson et al. (1981) estimated that Europa could be losing 100 m of surface ice per billion years due to sputtering, but the more hospitable charged particle flux at the location of the main ring (Morfill et al., 1980) could mean a slower loss rate closer to 1 m Gyr^{-1}. Although icy dust grains would be easily destroyed, a primordial 10-m (or larger) water ice ring parent body would survive over the age of the Solar System at these sputtering rates. So although it is unlikely that water ice could be a significant component of the dust grain population in the ring, it may be present on the larger parent bodies. The spectral slope of this feature is steeper than that of the 2-μm feature in Saturn's ring spectrum (dashed line in Fig. 11), and the "hump" in the jovian ring spectrum near 2.4 μm is absent from the saturnian ring spectrum. Features in Saturn's ring spectrum are due to water ice, so the difference between the spectra of the two ring systems argue weakly against the spectrally-identifiable presence of water ice in the jovian ring spectrum.

Please cite this article as: M.H. Wong et al., Ground-based near infrared spectroscopy of Jupiter's ring and moons, Icarus (2006), doi:10.1016/j.icarus.2006.07.007

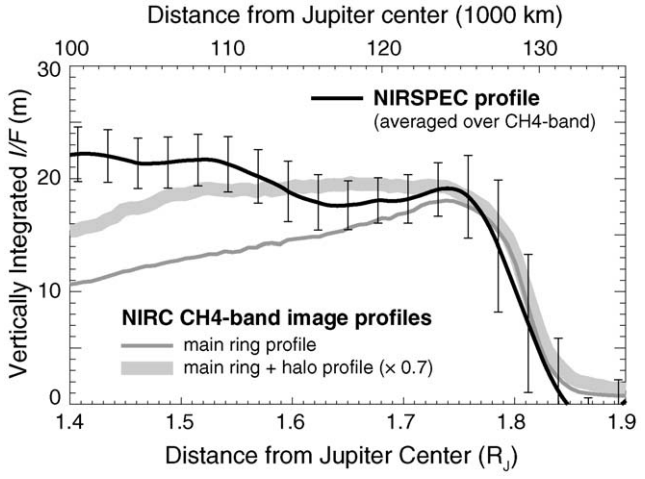

Fig. 12. Comparison of profiles derived from the NIRC CH4-band image with the NIRSPEC profile averaged over the same wavelength range. The NIRC profiles are the 2002 December profiles from Fig. 6, but the thick profile is scaled by a factor of 0.7 to allow easier shape comparison with the NIRSPEC profile. The closer match between the NIRSPEC profile and the thick profile can be explained by NIRSPEC oversampling of the halo contribution (see Section 3.2.2). NIRSPEC error bars show the effect of both systematic and statistical uncertainties. The profile has been Gaussian-smoothed with a half width of 0.62″ (0.03 R_J) to reduce noise.

3.2.2. Radial NIRSPEC profile

A radial profile of the ring, obtained by integrating the NIRSPEC spectrum over 2.20–2.35 μm (corresponding to the bandpass of the NIRC CH4-filter) is shown in Fig. 12. Fig. 12 also includes the ring plane profile (thin grey line) and the main ring + halo profile (thick grey line) derived from the December 2002 NIRC image. The shape of the NIRSPEC profile inwards of the ansa is much more similar to the shape of the thick CH4-band profile than the shape of the thin CH4-band profile, although the angular width of the spectrograph slit (0.76″) is equal to the width of the thin profile. The shape of the NIRSPEC profile suggests that the halo is oversampled in the data with respect to the main ring. Our NIRSPEC calibration star frames show a full width at half maximum of about 9.3 pixels, or 1.08″, in the spatial direction along the slit. If the same point spread function (in angular units) applies in the spatial direction perpendicular to the slit, then a significant fraction (about 40%) of the reflected flux from the main ring would go undetected. This undersampling effect would not affect the halo, because it is extended in the direction perpendicular to the slit. Imprecise centering of the ring plane along the slit axis create additional oversampling of the extended halo. Hence, the relative contribution of the halo to the NIRSPEC radial profile is larger than in the NIRC thin profile, and more similar to the NIRC thick profile. Note that the undersampling of the ring-plane flux density does not affect the flux density calibration of the spectrum, since the total NIRSPEC flux density integrated over the CH4 bandpass is bootstrapped from the CH4 image. The increase in the NIRSPEC profile inward from 1.6 R_J is probably an artifact caused by residual stray light from Jupiter.

3.3. Callisto and Amalthea

The disk-averaged L′-band albedo of Callisto itself was measured to be 0.11. This is slightly brighter than the 0.081 ± 0.013 predicted by the disk-averaged L′ photometric model of Tittemore and Sinton (1989), which includes longitudinal and phase-angle variation but does not account for the opposition surge, probably because their data set includes only one point at a phase angle less than 4°. Because Callisto was emerging from just behind Jupiter (the central meridian longitude varied from 1.4° to 2.6° W during our observations), we imaged half of the leading hemisphere (Fig. 4, left side of disk) and half of the trailing hemisphere. The phase angle ranged from 1.51° to 1.50°. The leading hemisphere is slightly darker, consistent with the hemispheric asymmetry observed by Calvin and Clark (1993) and Calvin et al. (1995), who found geometric albedos increasing from 0.10 to 0.13 across the 3.4–4.1-μm range (corresponding to the NIRC2 L′ filter) on the trailing hemisphere and from 0.06 to 0.095 on the leading hemisphere. Ground based spectral measurements of Callisto done by a number of other groups yield similar albedos: Pollack et al. (1978) found geometric albedos increasing from about 0.08 at 3.4 μm to about 0.14 at 4.1 μm, while Roush et al. (1990) found geometric albedos increasing from about 0.06 to about 0.10. Cassini VIMS data (McCord et al., 2004) and Galileo NIMS data (McCord et al., 1998) are more difficult to compare directly to our L′ image due to the difference in phase angle. Nevertheless, the NIMS data show that there is significant variation in the L′ albedo at much smaller scales than the hemispherical pattern noted previously from the ground; some evidence for this inhomogeneity can be seen in our L′ image (Fig. 4). As a resolved image at low phase, our observation provides a link between these resolved high-phase spacecraft observations and the unresolved ground-based photometry at low phase.

To verify the spectral slopes in our ring data, we sent our Amalthea spectrum through the same data reduction pipeline, except that the frames were aligned on the satellite instead of on Jupiter's limb. The background bias correction for the Amalthea data was derived from the sky level measured adjacent to the satellite on both sides, rather than from the data just beyond the ring ansa as for the ring frames. The resulting spectrum of Amalthea (with I/F calculated assuming a projected area of 8750 km^2) is shown in Fig. 13. We observe Amalthea to have a slight red slope between 2.2 and 2.5 μm. Near 3 μm, the albedo is much lower than in the 2.2 to 2.5 μm window. Data from the recent ground-based spectra obtained by Takato et al. (2004) are overlaid (dark grey curves), with the lighter grey shaded regions corresponding to their stated photometric uncertainties.

There is excellent agreement between these two ground-based data sets, which provide the only spectra of Amalthea at these wavelengths, since no spectra of the satellite from Galileo NIMS or Cassini VIMS have been published. The NIRSPEC spectrum was co-added from frames in which the trailing side of Amalthea occupied 98–82% of the visible fraction of the satellite. Takato et al. (2004) measured the spectrum of the trailing hemisphere of Amalthea at $\lambda < 2.5$ μm in 2004 with

Please cite this article as: M.H. Wong et al., Ground-based near infrared spectroscopy of Jupiter's ring and moons, Icarus (2006), doi:10.1016/j.icarus.2006.07.007

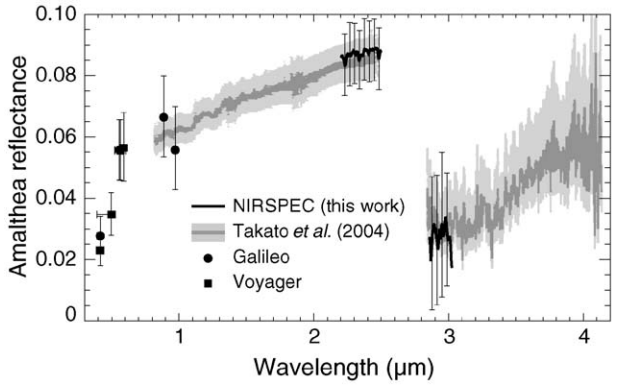

Fig. 13. Amalthea reflectance (black lines), assuming a cross-section of 8750 km^2. The spectrum is an average of frames taken as Amalthea moved inwards from ∼2.1 R_J to ∼1.6 R_J. Error bars show representative combined statistical and systematic uncertainties for several points in the spectrum. Amalthea's trailing hemisphere spectrum, from Takato et al. (2004), is plotted in dark grey for comparison; the light grey shading indicates their stated range of photometric uncertainty. Visible and near-IR reflectivities from analysis of Voyager and Galileo imaging data (Thomas et al., 1998) are shown, after adjustment for a phase angle of 8.9° using the Hapke reflectance model (Hapke, 1984, 1986, 1993) with parameters given by Simonelli et al. (2000).

SpeX at the IRTF and at $\lambda > 2.8$ μm with IRCS at the Subaru telescope in 2002–2003. Both spectral segments were photometrically scaled to match calibrated imaging data taken with IRCS, similar to our technique of scaling our NIRSPEC spectrum to calibrated NIRC imaging data. However, since we measured the 2.2–2.5 and 2.85–3.05 μm wavelength intervals within a single co-added spectrum, our result provides an important independent confirmation of the magnitude of the 3-μm absorption feature noted by Takato et al. (2004) and supports their inference of hydrated minerals and/or organics in the spectrum of the moonlet.

3.4. Broadband 1–4 μm ring spectrum

Fig. 11 places our Keck spectral observations in the context of other backscattered reflectance measurements from the visible to the infrared, reported within various wavelength intervals by numerous spacecraft and ground-based observers. Scaling corrections have been applied to correct for differences in viewing geometry, as described in Throop et al. (2004). At the 1.64-μm wavelength of our FeII data, we show normal reflectances derived from both our thin and thick profiles, and find that the main ring + halo point provides a better match to the previous observations (Neugebauer et al., 1981; Meier et al., 1999). Neugebauer et al. (1981) may have included a substantial amount of halo flux in their measurement (see Section 3.2.1). Meier et al. (1999) reported reflectances for the main ring only, but their HST data were acquired with a wide-band filter (F160W; FWHM = 0.4 μm), so if our reduced reflectance in the FeII filter is due to a narrow absorption feature, it would not be detected in the HST data. Although the scaling techniques of Throop et al. (2004) have facilitated the challenging task of comparing data obtained by several teams with different observational techniques, the Keck reflectance data in Fig. 11 avoid these issues by being consistently processed, so the main ring FeII data point can be combined with the CH4 imaging and spectroscopic data to show a strong red slope over the 1.6–2.4 μm region.

Our L′-band (3.4–4.1 μm) upper limit is the longest-wavelength constraint on the backscattered ring spectrum to date. Fig. 11 shows the 1-σ (black square) and 2-σ (upper error bar) upper limits for the L′ band, and it is clear that between 2 and 4 μm, the data support a spectrally flat slope or a blue slope. However, the L′-band upper limit precludes a continuation of the red spectral slope that extends from the visible to 2.4 μm. In Section 3.2.1, we noted that Throop et al. (2004) speculated that anomalously low large ring body reflectance at 2.2 μm could explain discrepancies between their model phase curve and the VIMS data at phase angles of 60°–120°. But since the VIMS data were co-added from spectral channels spanning 2.13–2.43 and 3.17–3.80 μm, it is arguably more likely that the difference between the VIMS phase curve and the Throop et al. (2004) model may instead be due to reduced large particle reflectance in the longer-wavelength VIMS range, a possibility that is consistent with our upper limit at L′-band.

The L′-band reflectivity upper limit raises the possibility of a spectral similarity between the main ring and Amalthea. Data from Takato et al. (2004) show that Amalthea's mean L′ spectral depression, relative to 2.5 μm, is about a 40% drop, but comparison with our main ring result is difficult since we have only an upper limit in the L′-band. The ring spectrum matches Amalthea's spectrum with a 40% or greater drop in the ring reflectance from 2.5 μm to L′-band, but only if the true ring reflectance is at or below the 1-σ noise level (L′ central data point in Fig. 11a). The spectral similarity between the main ring and Amalthea is clearer shortward of about 2.5 μm, where both have a red spectral slope (see Figs. 11 and 13; Throop et al., 2004; Takato et al., 2004). Depressed L′-band main ring reflectivity could indicate a significant contribution from large bodies in the ring, which may bear a spectral (and thus compositional) similarity to Amalthea. Laboratory reflectance spectra show that numerous common silicates such as olivine and pyroxene have large decreases in brightness between 2.5 and 4 μm. Takato et al. (2004) were skeptical of water ice as a candidate for explaining Amalthea's 3-μm absorption feature, because ice features at 2 and 1.5 μm were not seen in the spectrum of the moonlet.

4. Conclusions

The observations described here suggest that spectral features in Jupiter's ring system might help constrain ring particle compositions. The NIRSPEC main ring spectrum suggests an absorption feature at $\lambda < 2.25$ μm, which may have been missed by previous observations, all of which relied on photometry from images taken with broader-band filters. Future spectra must be acquired at shorter wavelengths to confirm this feature, since any quantitative analysis would need to measure a band center and width. We also obtained an upper limit for the ring's reflectance in the L′ filter (3.4–4.1 μm), which is consistent with a grey or blue spectral slope between 2.5 and 4 μm. The 1-σ upper limit in L′ is consistent with a deep absorption feature that is also seen in our spectrum of Amalthea. Both the 2.2 and 4 μm

Please cite this article as: M.H. Wong et al., Ground-based near infrared spectroscopy of Jupiter's ring and moons, Icarus (2006), doi:10.1016/j.icarus.2006.07.007

absorption features qualitatively suggest silicate and/or water ice compositions for the ring parent bodies.

We interpret the lack of phase-angle variation (over $\alpha = 1.2°–11.0°$) in our CH4-band main ring profiles to indicate irregular dust particles and/or regolith-free main ring parent bodies. Imaging at 1.64 and 2.27 μm shows these parent bodies to be redder than the halo particles.

Although this study makes the need for wider spectral coverage at higher spectral resolution quite apparent, we have found that the background light environment this close to Jupiter makes spectroscopy even more challenging than imaging, since the two-dimensional coverage in images makes background light correction more straightforward. Improvements in recent technology, including integral field spectrographs such as OSIRIS at Keck (Larkin et al., 2003) and SINFONI at the VLT (Eisenhauer et al., 2003), will greatly enhance the ability to determine the backscattered infrared spectral character of the ring. These instruments will combine high spectral resolution with two-dimensional spatial imaging, making stray light corrections much more accurate. Laser guide star adaptive optics may provide an ideal tool for ring observations, improving the sensitivity to the faint but compact ring by allowing longer integration times that are not limited by the availability of transient "guide stars" such as Callisto.

Uncited references

(Clark and McCord, 1980) (Moroz et al., 1999) (Schade et al., 2004)

Acknowledgments

We thank Henry Throop, whose thorough review improved this paper greatly, as well as an anonymous reviewer.

References

Acuña, M.H., Ness, N.F., 1976. The complex main magnetic field of Jupiter. J. Geophys. Res. 81, 2917–2922.

Banfield, D., Conrath, B.J., Gierasch, P.J., Nicholson, P.D., Matthews, K., 1998. Near-IR spectrophotometry of jovian aerosols-meridional and vertical distributions. Icarus 134, 11–23.

Bell, J.F., Owensby, P.D., Hawke, B.R., Gaffey, M.J., 1988. The 52-color asteroid survey: Final results and interpretation. Lunar Planet. Sci. Conf. 19, 57–58.

Brooks, S.M., Esposito, L.W., Showalter, M.R., Throop, H.B., 2004. The size distribution of Jupiter's main ring from Galileo imaging and spectroscopy. Icarus 170, 35–57.

Brown, R.H., Baines, K.H., Bellucci, G., Bibring, J.-P., Buratti, B.J., Capaccioni, F., Cerroni, P., Clark, R.N., Coradini, A., Cruikshank, D.P., Drossart, P., Formisano, V., Jaumann, R., Langevin, Y., Matson, D.L., McCord, T.B., Mennella, V., Nelson, R.M., Nicholson, P.D., Sicardy, B., Sotin, C., Amici, S., Chamberlain, M.A., Filacchione, G., Hansen, G., Hibbitts, K., Showalter, M., 2003. Observations with the visual and infrared mapping spectrometer (VIMS) during Cassini's flyby of Jupiter. Icarus 164, 461–470.

Burns, J.A., Showalter, M.R., Morfill, G.E., 1984. The ethereal rings of Jupiter and Saturn. In: Greenberg, Brahic (Eds.), Planetary Rings. Univ. of Arizona Press, Tucson, AZ.

Burns, J.A., Showalter, M.R., Hamilton, D.P., Nicholson, P.D., de Pater, I., Ockert-Bell, M.E., Thomas, P.C., 1999. The formation of Jupiter's faint rings. Science 284, 1146–1150.

Burns, J.A., Simonelli, D.P., Showalter, M.R., Hamilton, D.P., Porco, C.D., Throop, H., Esposito, L.W., 2004. Jupiter's ring–moon system. In: Bagenal, F., Dowling, T.E., McKinnon, W.B. (Eds.), Jupiter. The Planet, Satellites and Magnetosphere. Cambridge Univ. Press, Cambridge, UK, pp. 241–262.

Calvin, W.M., Clark, R.N., 1993. Spectral distinctions between the leading and trailing hemispheres of Callisto: New observations. Icarus 104, 68–78.

Calvin, W.M., Clark, R.N., Brown, R.H., Spencer, J.R., 1995. Spectra of the icy Galilean satellites from 0.2 to 5 μm: A compilation, new observations, and a recent summary. J. Geophys. Res. 100, 19041–19048.

Clark, R.N., McCord, T.B., 1980. The rings of Saturn—New near-infrared reflectance measurements and a 0.326–4.08 micron summary. Icarus 43, 161–168.

Colina, L., Bohlin, R.C., Castelli, F., 1996. The 0.12–2.5 micron absolute flux distribution of the Sun for comparison with solar analog stars. Astron. J. 112, 307–315.

de Pater, I., Showalter, M.R., Burns, J.A., Nicholson, P.D., Liu, M.C., Hamilton, D.P., Graham, J.R., 1999. Keck infrared observations of Jupiter's ring system near Earth's 1997 ring plane crossing. Icarus 138, 214–223.

Eisenhauer, F., Abuter, R., Bickert, K., Biancat-Marchet, F., Bonnet, H., Brynnel, J., Conzelmann, R.D., Delabre, B., Donaldson, R., Farinato, J., Fedrigo, E., Genzel, R., Hubin, N.N., Iserlohe, C., Kasper, M.E., Kissler-Patig, M., Monnet, G.J., Roehrle, C., Schreiber, J., Stroebele, S., Tecza, M., Thatte, N.A., Weisz, H., 2003. SINFONI—Integral field spectroscopy at 50 milliarcsecond resolution with the ESO VLT. In: Iye, M., Moorwood, A.F.M. (Eds.), Instrument Design and Performance for Optical/Infrared Ground-based Telescopes. In: Proc. SPIE, vol. 4841, pp. 548–1561.

Elias, J.H., Frogel, J.A., Matthews, K., Neugebauer, G., 1982. Infrared standard stars. Astron. J. 87, 1029–1034.

Fillius, R.W., McIlwain, C.E., Mogro-Campero, A., 1975. Radiation belts of Jupiter: A second look. Science 188, 465–467.

Gaffey, M.J., Burbine, T.H., Piatek, J.L., Reed, K.L., Chaky, D.A., Bell, J.F., Brown, R.H., 1993. Mineralogical variations within the S-type asteroid class. Icarus 106, 573–602.

Gerakines, P.A., Bray, J.J., Davis, A., Richey, C.R., 2005. The strengths of near-infrared absorption features relevant to interstellar and planetary ices. Astrophys. J. 620, 1140–1150.

Graham, J.R., Matthews, K., Soifer, B.T., Nelson, J.E., Harrison, W., Jernigan, J.G., Lin, S., Neugebauer, G., Smith, G., Ziomkowski, C., 1994. Infrared observations of the $Z = 3.8$ radio galaxy, 4C 41.17, with the W.M. Keck telescope. Astrophys. J. 420, L5–L8.

Hamilton, D.P., 1994. A comparison of Lorentz, planetary gravitational, and satellite gravitational resonances. Icarus 109, 221–240.

Hammel, H.B., Baines, K.H., Bergstralh, J.T., 1989. Vertical aerosol structure of Neptune—Constraints from center-to-limb profiles. Icarus 80, 416–438.

Hapke, B., 1993. Theory of Reflectance and Emittance Spectroscopy. Topics in Remote Sensing. Cambridge Univ. Press, Cambridge, UK.

Hapke, B., 1986. Bidirectional reflectance spectroscopy. IV. The extinction coefficient and the opposition effect. Icarus 67, 264–280.

Hapke, B., 1984. Bidirectional reflectance spectroscopy. III. Correction for macroscopic roughness. Icarus 59, 41–59.

Horányi, M., Cravens, T.E., 1996. The structure and dynamics of Jupiter's ring. Nature 381, 293–295.

Ip, W.-H., 1980. Discussion of the Pioneer 11 observations of the F ring of Saturn. Nature 287, 126–128.

Jewitt, D.C., Danielson, G.E., 1981. The jovian ring. J. Geophys. Res. 86, 8691–8697.

Johnson, R.E., Lanzerotti, L.J., Brown, W.L., Armstrong, T.P., 1981. Erosion of Galilean satellite surfaces by jovian magnetosphere particles. Science 212, 1027–1030.

Labs, D., Neckel, H., 1968. The radiation of the solar photosphere from 2000 Å to 100 μm. Z. Astrophys. 69, 1–73.

Labs, D., Neckel, H., 1970. Transformation of the absolute solar radiation data into the international practical temperature scale of 1968. Sol. Phys. 15, 79–87.

Larkin, J.E., Quirrenbach, A., Krabbe, A., Aliado, T., Barczys, M., Brims, G., Canfield, J., Gasaway, T.M., LaFreniere, D., Magnone, N., Skulason, G., Spencer, M., Sprayberry, D., Weiss, J., 2003. OSIRIS: Infrared integral field spectrograph for the Keck adaptive optics system. In: Iye, M., Moorwood,

A.F.M. (Eds.), Instrument Design and Performance for Optical/Infrared Ground-based Telescopes. In: Proc. SPIE, vol. 4841, pp. 1600–1610.

Liu, M.C., 2000. Distances and stellar populations of elliptical galaxies from surface brightness fluctuations. Bull. Amer. Astron. Soc. 32. 1500.

Liu, M.C., Graham, J.R., 2001. Infrared surface brightness fluctuations of the coma elliptical Galaxy NGC 4874 and the value of the Hubble constant. Astrophys. J. 557, L31–L34.

Matthews, K., Soifer, B.T., 1994. The near-infrared camera on the W.M. Keck telescope. In: McClean, I.S. (Ed.), Infrared Arrays in Astronomy: The Next Generation. Kluwer Academic, Dordrecht, pp. 239–246.

McCord, T.B., Hansen, G.B., Clark, R.N., Martin, P.D., Hibbitts, C.A., Fanale, F.P., Granahan, J.C., Segura, M., Matson, D.L., Johnson, T.V., Carlson, R.W., Smythe, W.D., Danielson, G.E., and the NIMS Team, 1998. Non-water–ice constituents in the surface material of the icy Galilean satellites from the Galileo near-infrared mapping spectrometer investigation. J. Geophys. Res. 103 (E4), 8603–8628.

McCord, T.B., Coradini, A., Hibbitts, C.A., Capaccioni, F., Hansen, G.B., Filacchione, G., Clark, R.N., Cerroni, P., Brown, R.H., Baines, K.H., Bellucci, G., Bibring, J.-P., Buratti, B.J., Bussoletti, E., Combes, M., Cruikshank, D.P., Drossart, P., Formisano, V., Jaumann, R., Langevin, Y., Matson, D.L., Nelson, R.M., Nicholson, P.D., Sicardy, B., Sotin, C., 2004. Cassini VIMS observations of the Galilean satellites including the VIMS calibration procedure. Icarus 172, 104–126.

McLean, I.S., Becklin, E.E., Bendiksen, O., Brims, G., Canfield, J., Figer, D.F., Graham, J.R., Hare, J., Lacayanga, F., Larkin, J.E., Larson, S.B., Levenson, N., Magnone, N., Teplitz, H., Wong, W., 1998. Design and development of NIRSPEC: A near-infrared Echelle spectrograph for the Keck II telescope. In: Fowler, A.M. (Ed.), Infrared Astronomical Instrumentation. In: Proc. SPIE, vol. 3354, pp. 566–578.

McMuldroch, S., Pilorz, S.H., Danielson, G.E., and the NIMS Science Team, 2000. Galileo NIMS near-infrared observations of Jupiter's ring system. Icarus 146, 1–11.

Meier, R., Smith, B.A., Owen, T.C., Becklin, E.E., Terrile, R.J., 1999. Near infrared photometry of the jovian ring and Adrastea. Icarus 141, 253–262.

Mishchenko, M.I., Travis, L.D., 1998. Capabilities and limitations of a current FORTRAN implementation of the T-matrix method for randomly oriented, rotationally symmetric scatterers. J. Quant. Spectrosc. Radiat. Trans. 60 (3), 309–324.

Morfill, G.E., Gruen, E., Johnson, T.V., 1980. Dust in Jupiter's magnetosphere: Physical processes. Planet. Space Sci. 28, 1087–1123.

Moroz, L.V., Schade, U., Wäsch, R., 1999. Near-infrared reflectance spectra of olivine–orthopyroxene mixtures and ordinary chondrites at low temperatures. Meteorit. Planet. Sci. 34. Supplement 83.

Neugebauer, G., Becklin, E.E., Jewitt, D.C., Terrile, R.J., Danielson, G.E., 1981. Spectra of the jovian ring and Amalthea. Astron. J. 86, 607–610.

Nicholson, P.D., Matthews, K., 1991. Near-infrared observations of the jovian ring and small satellites. Icarus 93, 331–346.

Nicholson, P.D., Showalter, M.R., Dones, L., French, R.G., Larson, S.M., Lissauer, J.J., McGhee, C.A., Sicardy, B., Seitzer, P., Danielson, G.E., 1996. Observations of Saturn's ring-plane crossing in August and November. Science 272, 509–516.

Ockert-Bell, M.E., Burns, J.A., Dauber, I.J., Thomas, P.C., Veverka, J., Belton, M.J.S., Klaasen, K.P., 1999. The structure of Jupiter's ring system as revealed by the Galileo imaging experiment. Icarus 138, 188–213.

Owen, T., Danielson, G.E., Cook, A.F., Hansen, C., Hall, V.L., Duxbury, T.C., 1979. Jupiter's rings. Nature 281, 442–446.

Persson, S.E., Murphy, D.C., Krzeminski, W., Roth, M., Rieke, M.J., 1998. A new system of faint near-infrared standard stars. Astron. J. 116, 2475–2488.

Pollack, J.B., Witteborn, F.C., Erickson, E.F., Strecker, D.W., Baldwin, B.J., Reynolds, R.T., 1978. Near-infrared spectra of the Galilean satellites: Observations and compositional implications. Icarus 36, 271–303.

Porco, C.C., West, R.A., McEwen, A., DelGenio, A.D., Ingersoll, A.P., Thomas, P., Squyres, S., Dones, L., Murray, C.D., Johnson, T.V., Burns, J.A., Brahic, A., Neukum, G., Veverka, J., Barbara, J.M., Denk, T., Evans, M., Ferrier, J.J., Geissler, P., Helfenstein, P., Roatsch, T., Throop, H., Tiscareno, M., Vasavada, A., 2003. Cassini imaging of Jupiter's atmosphere, satellites, and rings. Science 299, 1541–1547.

Rajaram, B., Glandorf, D.L., Curtis, D.B., Tolbert, M.A., Toon, O.B., Ockman, N., 2001. Temperature-dependent optical constants of water ice in the near infrared: New results and critical review of the available measurements. Appl. Opt. 40, 4449–4462.

Roush, T.L., Pollack, J.B., Witteborn, F.C., Bregman, J.D., Simpson, J.P., 1990. Ice and minerals on Callisto: A reassessment of the reflectance spectra. Icarus 86, 355–382.

Schade, U., Wäsch, R., Moroz, L., 2004. Near-infrared reflectance spectroscopy of Ca-rich clinopyroxenes and prospects for remote spectral characterization of planetary surfaces. Icarus 168, 80–92.

Schaffer, L., Burns, J.A., 1992. Lorentz resonances and the vertical structure of dusty rings—Analytical and numerical results. Icarus 96, 65–84.

Showalter, M.R., Burns, J.A., Cuzzi, J.N., Pollack, J.B., 1985. Discovery of Jupiter's 'gossamer' ring. Nature 316, 526–528.

Showalter, M.R., Burns, J.A., Cuzzi, J.N., Pollack, J.B., 1987. Jupiter's ring system: New results on structure and particle properties. Icarus 69, 458–498.

Showalter, M.R., de Pater, I., Verbanac, G., Hamilton, D.P., Burns, J.A., 2006. Properties and dynamics of Jupiter's gossamer rings from Galileo, Voyager, Hubble and Keck images. Icarus. In preparation.

Simonelli, D.P., Rossier, L., Thomas, P.C., Veverka, J., Burns, J.A., Belton, M.J.S., 2000. Leading/trailing albedo asymmetries of Thebe, Amalthea, and Metis. Icarus 147, 353–365.

Smoluchowski, R., 1976. Origin and structure of Jupiter and its satellites. In: Gehrels, T. (Ed.), Jupiter. Univ. of Arizona Press, Tucson, AZ, pp. 3–21.

Squyres, S.W., Veverka, J., 1981. Voyager photometry of surface features on Ganymede and Callisto. Icarus 46, 137–155.

Takato, N., Bus, S.J., Terada, H., Pyo, T., Kobayashi, N., 2004. Detection of a deep 3-μm absorption feature in the spectrum of Amalthea (JV). Science 306, 2224–2227.

Thomas, P.C., Burns, J.A., Rossier, L., Simonelli, D., Veverka, J., Chapman, C.R., Klaasen, K., Johnson, T.V., Belton, M.J.S., 1998. The small inner satellites of Jupiter. Icarus 135, 360–371.

Throop, H.B., Porco, C.C., West, R.A., Burns, J.A., Showalter, M.R., Nicholson, P.D., 2004. The jovian rings: New results derived from Cassini, Galileo, Voyager, and Earth-based observations. Icarus 172, 59–77.

Tittemore, W.C., Sinton, W.M., 1989. Near-infrared photometry of the Galilean satellites. Icarus 77, 82–97.

Warren, S.G., 1984. Optical constants of ice from the ultraviolet to the microwave. Appl. Opt. 23, 1206–1225.

Please cite this article as: M.H. Wong et al., Ground-based near infrared spectroscopy of Jupiter's ring and moons, Icarus (2006), doi:10.1016/j.icarus.2006.07.007